Rotation sensing with improved stability using point source atom interferometry

Chen Avinadav, ^{1, 2, *} Dimitry Yankelev, ^{1, 2, †} Moshe Shuker, ² Nir Davidson, ¹ and Ofer Firstenberg ¹ Department of Physics of Complex Systems, Weizmann Institute of Science, Rehovot 7610001, Israel ² Rafael Ltd, Haifa 3102102, Israel

Point source atom interferometry is a promising approach for implementing robust, high-sensitivity, rotation sensors using cold atoms. However, its scale factor, *i.e.*, the ratio between the interferometer signal and the actual rotation rate, depends on the initial conditions of the atomic cloud, which may drift in time and result in bias instability, particularly in compact devices with short interrogation times. We present two methods to stabilize the scale factor, one relying on a model-based correction which exploits correlations between multiple features of the interferometer output and works on a single-shot basis, and the other a self-calibrating method where a known bias rotation is applied to every other measurement, requiring no prior knowledge of the underlying model but reducing the sensor bandwidth by a factor of two. We demonstrate both schemes experimentally with complete suppression of scale factor drifts, maintaining the original rotation sensitivity and allowing for bias-free operation over several hours.

Cold atom interferometers [1] have achieved in recent years record sensitivities in acceleration and rotation sensing. As acceleration-sensing instruments, their applications range from precision measurements for fundamental research [2–10] to geophysical measurements with mobile atomic gravimeters [11–18], demonstrating both high sensitivity and high stability operation. Atom interferometry gyroscopes [19–24] are useful for field applications such as gyrocompassing [25, 26] and inertial navigation on mobile platforms [27, 28]. Point source interferometry (PSI) is an especially promising approach for such applications.

PSI is an atom interferometry technique for rotation sensing based on detecting the frequency of a spatial interference pattern across an atomic cloud. Originally developed in a 10-meter atomic fountain [22], the technique has also been applied in a sensor with cm-scale physics package [24, 29]. Compared to other atom interferometry rotation sensing techniques, PSI has the benefits of experimental simplicity and inherent suppression of accelerations and vibrations. However, the scale factor of PSI is sensitive to the initial and final size of the atomic cloud, especially when the expansion ratio is small as in compact sensors with short expansion times [29]. As a result, PSI is susceptible to bias instability due to drifts in these technical attributes of the atomic sensor, limiting its usefulness in applications requiring high stability over long time scales.

In this work, we introduce two approaches to stabilizing scale-factor drifts in PSI measurements. The first approach utilizes additional information extracted from each PSI image, namely the interference fringe contrast and atomic cloud final size, in addition to the fringe frequency. Exploiting the correlation between these parameters, we determine the scale factor correction for every PSI image independently. The second approach relies on alternately applying a known bias rotation rate to the sensor, in addition to the unknown measured rotation. Analyzing pairs of measurements with and without the

bias rotation enables self-calibration of the scale factor correction and determination of the unknown rotation. We implement both schemes experimentally and demonstrate their ability to recover uncorrelated $\tau^{-1/2}$ performance of the rotation sensor and suppress scale factor drifts up to a factor of ten without any loss in sensitivity.

Generally, PSI employs a Mach-Zehnder atom interferometer configuration [30], where three laser pulses, equally separated in time, interact with a freely-falling atomic cloud to split, redirect, and recombine the atomic wavepackets in space (Fig. 1). In our apparatus [31, 32], we trap an ensemble of ⁸⁷Rb atoms in a magneto-optical trap and cool them down to $4\,\mu\rm K$. Through moving optical molasses, the atoms are launched vertically at velocities of up to $1.2\,\rm m/s$ while occupying all Zeeman states $m_F=0,\pm 1$ of the lower hyperfine level F=1. The in-

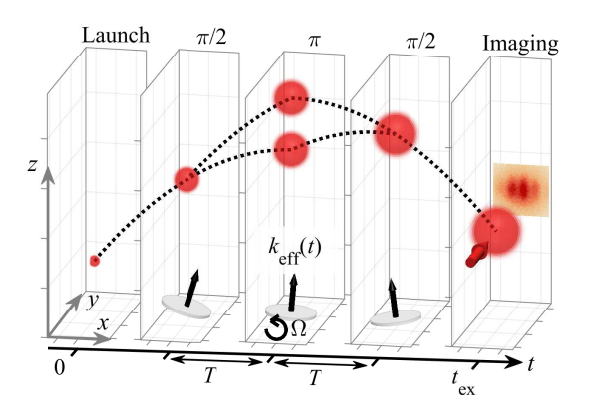


Figure 1. Schematic diagram of point source atom interferometry. The atomic cloud is launched upwards at t=0, interacts with a sequence of $\pi/2$ - π - $\pi/2$ two-photon Raman pulses comprising the interferometer, and finally imaged at $t=t_{\rm ex}$. The effective wave vector ${\bf k}_{\rm eff}$ of the counter-propagating Raman beams is determined by a retro-reflecting mirror which can be tilted by a piezo stage to simulate rotations. Ballistic expansion of the cloud generates correlation between position and velocity of the atoms, giving rise to a spatial interference pattern from which the rotation rate is calculated.

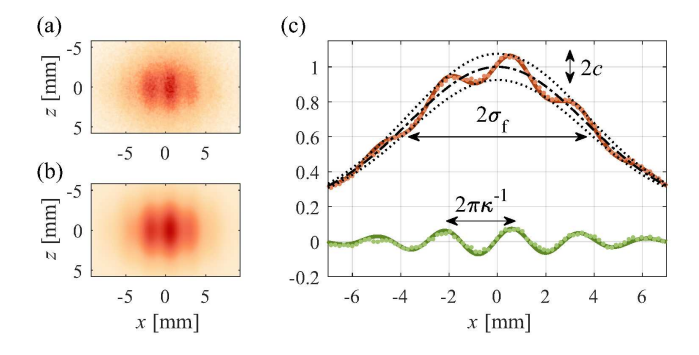


Figure 2. Spatial fringe pattern measured with PSI. (a) Raw fluorescence image from a single experiment. (b) Fit of the image to a two-dimensional Gaussian distribution with sinusoidal modulation. (c) Normalized, vertically integrated cross sections of the measured and fitted images (red dotted and solid lines, respectively). The Gaussian density distribution (dash-dotted line) of full width $2\sigma_{\rm f}$ is modulated by a fringe pattern (green) with spatial frequency κ and contrast c.

terferometer pulses are realized by counter-propagating Raman beams that drive two-photon transitions between the $m_F = 0$ states of F = 1 and F = 2. Following the pulse sequence, we use fluorescence excitation on the optical $F = 2 \rightarrow F' = 3$ cycling transition to capture an image of the atoms occupying the F = 2 level.

The leading contributions to the interferometer phase are given by $\phi_{\mathbf{a}} = \mathbf{k}_{\text{eff}} \cdot \mathbf{a} T^2$ and $\phi_{\Omega} = 2\mathbf{k}_{\text{eff}} \cdot (\mathbf{\Omega} \times \mathbf{v}) T^2$, where $\mathbf{k}_{\text{eff}} = \mathbf{k}_1 - \mathbf{k}_2$ is the two-photon wave vector of the Raman laser beams, T is the time between each pair of pulses, \mathbf{a} and $\mathbf{\Omega}$ are respectively the acceleration and rotation rate of the atoms relative to the retro-reflecting mirror, and \mathbf{v} is the mean velocity of each atom during the interferometer sequence. In our setup, $\mathbf{k}_{\text{eff}} = k_{\text{eff}} \hat{\mathbf{z}}$ and the cloud is imaged in the $\hat{\mathbf{x}}$ - $\hat{\mathbf{z}}$ plane, providing sensitivity to rotations only around the $\hat{\mathbf{y}}$ axis. For simplicity we denote $\Omega = \Omega_y$ and write the rotation phase term as $\phi_{\Omega} = 2k_{\text{eff}}\Omega v_x T^2$. The Raman retro-reflecting mirror is mounted on a tip-tilt piezo stage, which allows us to rotate the Raman wave-vector during the interferometer sequence and thereby mimic actual rotations.

While $\phi_{\mathbf{a}}$ is uniform across the expanding atomic cloud, ϕ_{Ω} depends on initial transverse velocity of each atom. In the point-source limit, where the magnification ratio of final to initial cloud size is infinite, ballistic expansion of the cloud creates perfect correlations between the atomic position and velocity, $x = v_x t_{\mathrm{ex}}$, where t_{ex} is the total expansion time. Thus we may write $\phi_{\Omega} = \kappa\left(\Omega\right)x$, representing a spatial fringe pattern with frequency $\kappa\left(\Omega\right) = F\Omega$, where the scale factor in the point-source limit is given by $F_{\mathrm{ps}} = 2k_{\mathrm{eff}}T^2/t_{\mathrm{ex}}$ [22]. The resulting atomic density profile consists of a Gaussian envelope with sinusoidal modulation, as shown in Fig. 2.

At finite magnification ratios, the final atomic density profile is a convolution of the ideal point-source fringe pattern with the initial density distribution. The scale factor is predicted to change as $F = F_{\rm ps}(1 - \sigma_{\rm i}^2/\sigma_{\rm f}^2)$, assuming spherically-symmetric Gaussian initial and final density distributions of widths $\sigma_{\rm i}$ and $\sigma_{\rm f}$, respectively [33]. Consequently, the sensed rotation rate as a function of the measured fringe frequency κ becomes

$$\Omega = \frac{\kappa}{F_{\rm ps} \left(1 - \sigma_{\rm i}^2 / \sigma_{\rm f}^2\right)}.\tag{1}$$

The dependency on σ_i/σ_f leads to bias instability of the sensor when either σ_i or σ_f drift. Importantly, for a given relative drift in σ_i , the drift in the scale factor increases with the inverse magnification ratio σ_i/σ_f , emphasizing the susceptibility of compact sensors with small magnification to such drifts.

In the following, we shall use the fact that σ_i and σ_f also affect the fringe contrast c. It is given, under the above assumption, by [33]

$$c = c_0 \exp\left[-\frac{1}{2} \frac{\kappa^2 \sigma_i^2}{1 - \sigma_i^2 / \sigma_\ell^2}\right],\tag{2}$$

where c_0 is the interferometer contrast for $\Omega = 0$.

We verify the model predictions by performing measurements with different values of σ_i , obtained through different repump intensities at the final optical molasses

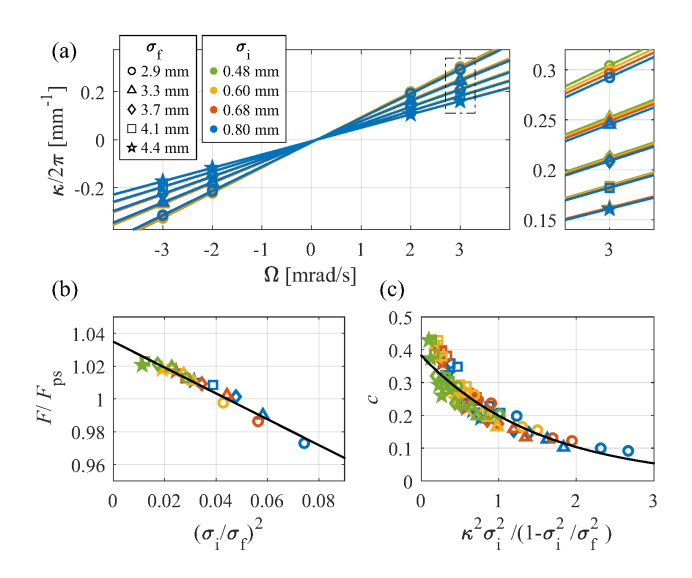


Figure 3. Effect of initial cloud size $\sigma_{\rm i}$ and final cloud size $\sigma_{\rm f}$ on PSI scale factor and contrast. (a) Measured fringe frequency κ as a function of Ω for different values of $\sigma_{\rm i}$ and $\sigma_{\rm f}$. Solid lines are linear fits, with slopes representing the scale factors. Different values of $\sigma_{\rm f}$ correspond to launch velocities 0.6-1.2 m/s, with $t_{\rm ex}$ between 133-252 ms. In all cases T=52 ms. (b) Measured scale factor for different values of $\sigma_{\rm i}$ and $\sigma_{\rm f}$. Solid line is a linear fit with slope -0.79(4), deviating from the predicted value -1. (c) Measured fringe contrast for different values of $\sigma_{\rm i}$ and $\sigma_{\rm f}$. Solid line is an exponential fit to $c=c_0\exp\left[-\alpha\kappa^2\sigma_{\rm i}^2/\left(1-\sigma_{\rm i}^2/\sigma_{\rm f}^2\right)\right]$ with $\alpha=0.65(3)$, deviating from the model prediction $\alpha=0.5$.

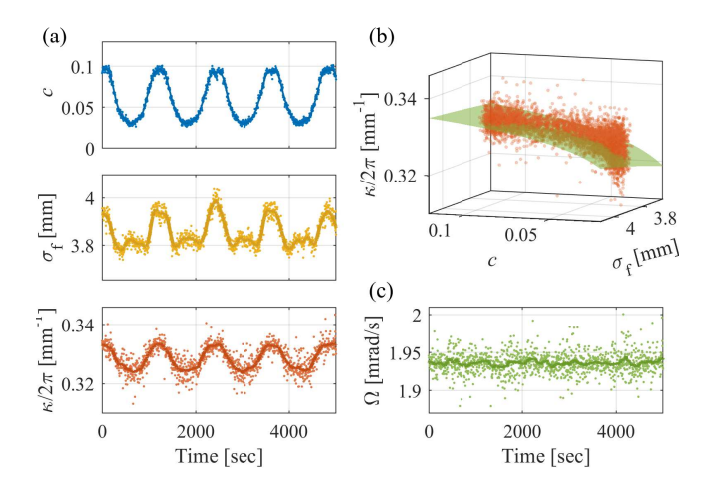


Figure 4. Calibration of contrast-based scale-factor stabilization. (a) Top to bottom: measured contrast, final cloud size, and fringe frequency, as σ_i is varied periodically. Each data point represents a single PSI image. In these and following experiments, $T=80\,\mathrm{ms}$ and $t_\mathrm{ex}=185\,\mathrm{ms}$. (b) Parametric plot of $\kappa\left(c,\sigma_\mathrm{f}\right)$. Dots are data points, surface is a fit to Eq. (4) with $c_0=0.43(8)$ and $\beta=0.80(1)$. (c) Rotation rate calculated from Eq. (3), showing elimination of scale-factor drifts. Solid lines in (a),(c) are 30-samples moving averages.

stage, and with different values $\sigma_{\rm f}$, obtained through different launch velocities and thus different expansion times. $\sigma_{\rm i}$ was measured in independent experiments by imaging the cloud immediately after launch. As Fig. 3 shows, we find good agreement with the functionals in Eqs. (1-2) for a range of magnification ratios $\sigma_{\rm f}/\sigma_{\rm i}$ between 3.5 and 9. The fitted slope for the scale factor dependence on $\sigma_{\rm i}^2/\sigma_{\rm f}^2$, as well as the scaling of the exponential decrease of the contrast, slightly differ from the theoretical model either due to estimation errors in $\sigma_{\rm i}$ and $\sigma_{\rm f}$, or due to non-Gaussian density distributions. The fact that the scale factor F at $\sigma_{\rm i}/\sigma_{\rm f} \rightarrow 0$ differs from $F_{\rm ps}$ by 3.5% can be attributed to a calibration errors of the imaging system and the piezo stage driving the mirror rotations.

The first method we present for correcting scale factor instability exploits the correlation between Ω and (κ, c, σ_f) which are extracted from each PSI image. From Eqs. (1-2), we obtain an expression for Ω ,

$$\Omega = \frac{\kappa}{F_{\rm ps}} \left[1 - 2 \left(\frac{\beta}{\kappa \sigma_{\rm f}} \right)^2 \ln \frac{c}{c_0} \right], \tag{3}$$

where c_0 and β are calibration parameters, with β added to capture the aforementioned deviations from the model. We verify empirically that this formulation is sufficient to describe the measured data. Importantly, it allows us to calculate Ω using only the parameters κ , c and $\sigma_{\rm f}$ measured in every single PSI image, enabling analysis on a per-shot basis without any reduction in temporal bandwidth.

To calibrate c_0 and β in Eq. (3) we perform measurements at a constant rotation rate and periodically vary σ_i by changing the repump beam intensity during the moving optical molasses. This results in changes to c, σ_f , and κ , as shown in Fig. 4(a). Inverting Eq. (3), we obtain an expression for κ ,

$$\kappa = \frac{1}{2} F_{\rm ps} \Omega_{\rm calib} \left[1 + \sqrt{1 + \frac{8 \ln (c/c_0)}{(F_{\rm ps} \Omega_{\rm calib} \sigma_{\rm f}/\beta)^2}} \right]. \tag{4}$$

The measured data points are fitted to this surface equation, as shown in Fig. 4(b), with c_0 , β , and Ω_{calib} being fit parameters. The latter is an auxiliary parameter, not used in any subsequent analysis, which is allowed to deviate from the input rotation rate to account for Earth's rotation, possible errors in the piezo stage, and wavefront aberrations [25, 34, 35]. With calibrated c_0 and β at hand, we may use Eq. (3) to correct the inferred rotation rate in this calibration run. This exercise is shown in Fig. 4(c), and indeed we find that the drifts are removed and a stable rotation measurement is obtained. We emphasize that the analysis does not use any assumption or prior knowledge on σ_i or on its temporal variations, and in fact the only prerequisite is that the range of σ_i scanned during the calibration process is large enough to adequately calibrate the model parameters.

We demonstrate the implementation of this stabilization method in two separate measurement runs, as presented in Fig. 5, representing realistic operating scenarios where the rotation rate varies in time. We artificially generate scale-factor drifts by varying the optical molasses parameters which affect the initial and final cloud distributions, both in periodic fashion and in random-walk-like behavior. While the rotation rate and initial conditions change smoothly in time, this information is not used in the analysis as all corrections are on a single-shot basis. The interferometer parameters are $T=80\,\mathrm{ms}$ and $t_\mathrm{ex}=185\,\mathrm{ms}$, as in the calibration run.

Using Eq. (3) and the previously calibrated values for c_0 and β , we obtain suppression of sensor drifts by a factor of ten in both examples [Fig. 5(d),(h)], limited only by the magnitude of the drifts we introduced. The second example, where Ω varies around a different mean value than Ω_{calib} , demonstrates the technique generality and robustness. The scheme allows complete recovery of $\tau^{-1/2}$ averaging performance at time scales up to 10^4 seconds, affirming that it does not introduce new drifts of its own.

We note that it is possible to apply this correction approach by directly measuring σ_i in separate experimental shots and utilizing Eq. (1). We have successfully implemented this technique with similar results. The price, however, is a reduced bandwidth and sensitivity per $\sqrt{\text{Hz}}$ due to the interleaved dedicated measurements of σ_i and the added constraint on the allowed bandwidth of σ_i variation.

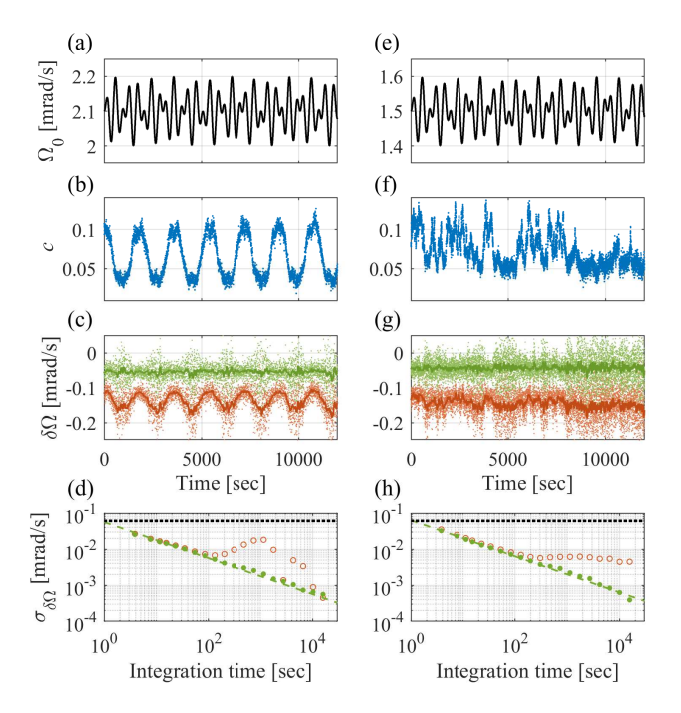


Figure 5. Demonstration of contrast-based scale-factor stabilization. (a) Time series of the input rotation rate Ω_0 , oscillating around 2.1 mrad/s. (b) Measured fringe contrast shows variations due to applied periodic changes to σ_i . (c) Residuals of the estimated rotation rate $\Omega - \Omega_0$, with (green) and without (red) scale-factor correction using Eq. (3). Solid lines are 30-samples moving averages. The full data spans 3×10^4 sec. (d) Allan deviation of the residuals, with and without scale factor correction. Dashed line is a fit to $\tau^{-1/2}$ with sensitivity $28 \, \mu \text{rad/s}$ per shot. Dotted line indicates Earth rotation rate at our lab location. (e-h) Same as (a-d), with Ω_0 oscillating around 1.5 mrad/s and random-walk variations in σ_i .

Our second method for scale-factor stabilization utilizes the piezo rotation stage to apply a known rotation Ω_{bias} at alternating measurements, in addition to the unknown rotation Ω which we wish to measure. Denoting the scale factor in these measurements as F, the spatial fringe frequencies of two consecutive measurements are given by $\kappa_1 = F\Omega$ and $\kappa_2 = F(\Omega + \Omega_{\text{bias}})$. These equations may be inverted to yield

$$\Omega = \Omega_{\text{bias}} \frac{\kappa_1}{\kappa_2 - \kappa_1},\tag{5}$$

$$F = \frac{1}{\Omega_{\text{bias}}} \left(\kappa_2 - \kappa_1 \right), \tag{6}$$

allowing us to extract both Ω and F from each pair of measurements κ_1 and κ_2 . This self-calibrating method requires no prior knowledge or assumption of a model describing the relationship between F and other system parameters.

The sensitivity in determining the scale factor, and thus the rotation rate, improves as $|\kappa_1 - \kappa_2|$ increases. Consequently the optimal selection for Ω_{bias} is such that κ_2 and κ_1 have opposite signs, with $|\kappa_2|$ having its maxi-

mal value within the detection bandwidth of PSI. Choosing Ω_{bias} may be done in real-time after κ_1 is measured and a rough estimate of Ω and F is available. The signs of κ_1, κ_2 are not directly available from the PSI images but rather assumed to be known, for example from an auxiliary rotation sensor.

An experimental demonstration of the self-calibration method is shown in Fig. 6, with both the measured rotation Ω and the scale factor changing in time. Again we find perfect suppression of scale factor drifts and recovery of $\tau^{-1/2}$ noise behavior. Compared to the previously described contrast-based stabilization, this method reduces the effective bandwidth by a factor of two due to the pairwise analysis but has the advantages of being model-independent and not requiring any initial calibration measurements. We note that despite the reduction in bandwidth, information is not lost when analyzing pairs of measurements and thus the rotation sensitivity per $\sqrt{\text{Hz}}$ is maintained, as evident in Fig. 6(e).

The analysis above assumes that Ω does not change significantly within each pair of measurements with respect to the inherent measurement uncertainty. This

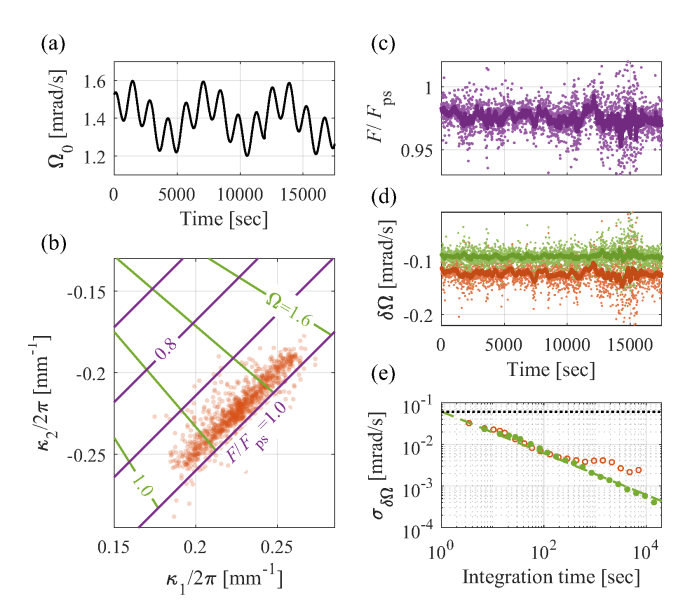


Figure 6. Demonstration of scale-factor stabilization by self-calibration. (a) Time series of the input rotation rate Ω_0 . (b) Measured κ_2 and κ_1 , each dot corresponding to a pair of experiments with and without $\Omega_{\text{bias}} = -2.6 \,\text{mrad/s}$. Also shown are contour lines of the estimated rotation rate (green) and scale factor correction relative to F_{ps} (purple) based on Eqs. (5-6). (c) Estimated scale factor correction from each pair of measurements, showing random-walk variations due to applied changes to σ_i . (d) Residuals of the estimated rotation rate $\Omega - \Omega_0$, using the nominal scale factor $F = F_{\text{ps}}$ (red) and the corrected scale factor (green). Solid lines in (c),(d) are 30-samples moving averages. (e) Allan deviation of the residuals, with and without scale factor correction. Dashed line is a fit to $\tau^{-1/2}$ with sensitivity $32 \,\mu\text{rad/s}$ per shot.

requirement may be relaxed by implementing more advanced estimation protocols, such as a Kalman filter [36], which would track rapidly varying rotation signals while estimating the slowly-varying scale factor from multiple measurement pairs. The self-calibration scheme also relies on an accurate piezo stage for adding a known bias rotation. However, such a stage with adequate performance is likely to be necessary anyway in an operational rotation sensor, for purposes such as calibration and dynamic range compensation.

In conclusion, we presented two complementary approaches for improving the stability of rotation measurements using point source atom interferometry, suppressing scale factor drifts which may arise due to changes in the atomic cloud parameters. One approach utilizes the inherent correlations between different parameters in PSI images for estimating the scale factor from a single image and correct for drifts. The underlying model which describes this correlation was verified by independent measurements. The second approach relies on sequential measurements with an added bias rotation to directly estimate the scale factor in a self-calibrating, model-independent way.

We demonstrated the two schemes experimentally with complete suppression of scale factor drifts, and showed that they maintain the sensor sensitivity and do not introduce any drifts on their own on time scales up to 10^4 sec and rotation rate stability of $0.5 \,\mu \mathrm{rad/s}$.

While the experiments described here focus on sideimaging PSI which allows single-axis rotation sensing, the two schemes we developed are fully compatible under the same conditions with dual-axis sensors using top- or bottom- imaging of the cloud.

These stabilization techniques are expected to be particularly important in compact PSI sensors which are more susceptible to scale factor drifts due to the low magnification ratio of the atomic cloud. Furthermore, in situations where the signal-to-noise ratio does not enable scale factor correction based on a single or a pair of PSI images, techniques such as Kalman or particle filtering may be used to optimally estimate the scale factor variations in time while maintaining high sensor bandwidth.

This work was supported by the Pazy Foundation, the Israel Science Foundation and the Quantum Technologies Development Consortium (RA). We thank Shlomi Kotler for fruitful discussions.

C.A. and D.Y. contributed equally to this work.

- * Electronic address: chen.avinadav@weizmann.ac.il.
- † Electronic address: dimitry.yankelev@weizmann.ac.il
- [1] G. M. Tino and M. A. Kasevich, eds., Atom Interferometry, in Proceedings of the International School of Physics

- "Enrico Fermi," Course CLXXXVIII (Societa Italiana di Fisica and IOS Press, 2014).
- [2] D. S. Weiss, B. C. Young, and S. Chu, Physical Review Letters 70, 2706 (1993).
- [3] S. Dimopoulos, P. W. Graham,
 J. M. Hogan, and M. A. Kasevich,
 Physical Review Letters 98 (2007), 10.1103/physrevlett.98.111102.
- [4] H. Müller, A. Peters, and S. Chu, Nature 463, 926 (2010).
- [5] R. Bouchendira, P. Cladé, S. Guellati-Khélifa, F. Nez, and F. Biraben, Physical Review Letters 106 (2011), 10.1103/physrevlett.106.080801
- [6] G. Rosi, F. Sorrentino, L. Cacciapuoti, M. Prevedelli, and G. M. Tino, Nature 510, 518 (2014).
- Zhou. S. Long, В. Tang, L. F. Gao, W. Peng, W. Duan, J. Zhong, Y. Zhang, and M. Zhan, Z. Xiong, J. Wang, Physical Review Letters 115 (2015), 10.1103/physrevlett.115.013004
- [8] B. Barrett, L. Antoni-Micollier, L. Chichet, B. Battelier, T. Lévèque, A. Landragin, and P. Bouyer, Nature Communications 7 (2016), 10.1038/ncomms13786.
- [9] R. H. Parker, C. Yu, W. Zhong, B. Estey, and H. Müller, Science 360, 191 (2018).
- [10] D. Becker, M. D. Lachmann, S. T. Seidel, H. Ahlers, A. N. Dinkelaker, J. Grosse, O. Hellmig, H. Müntinga, V. Schkolnik, T. Wendrich, A. Wenzlawski, B. Weps, R. Corgier, T. Franz, N. Gaaloul, W. Herr, D. Lüdtke, M. Popp, S. Amri, H. Duncker, M. Erbe, A. Kohfeldt, A. Kubelka-Lange, C. Braxmaier, E. Charron, W. Ertmer, M. Krutzik, C. Lämmerzahl, A. Peters, W. P. Schleich, K. Sengstock, R. Walser, A. Wicht, P. Windpassinger, and E. M. Rasel, Nature 562, 391 (2018).
- [11] K. Bongs, M. Holynski, J. Vovrosh, P. Bouyer, G. Condon, E. Rasel, C. Schubert, W. P. Schleich, and A. Roura, Nature Reviews Physics 1, 731 (2019).
- [12] X. Wu, Gravity Gradient Survey with a Mobile Atom Interferometer, Ph.D. thesis, Stanford (2009).
- [13] T. Farah, C. Guerlin, A. Landragin, P. Bouyer, S. Gaffet, F. P. D. Santos, and S. Merlet, Gyroscopy and Navigation 5, 266 (2014).
- [14] C. Μ. Schkolnik, Freier, Hauth, V. В. Leykauf, M. Schilling, Wziontek, G. Scherneck, J. Müller, and Α. Journal of Physics: Conference Series **723**, 012050 (2016).
- [15] V. Ménoret, P. Vermeulen, N. Le Moigne, S. Bonvalot, P. Bouyer, A. Landragin, and B. Desruelle, Scientific Reports 8, 12300 (2018).
- [16] Y. Bidel, C. Blanchard, N. Zahzam, Α. Bonnin, Μ. Cadoret, Α. Bresson, D. Rouxel, and M. F. Lequentrec-Lalancette, Nature Communications 9 (2018), 10.1038/s41467-018-03040-2.
- [17] X. Wu, Z. Pagel, B. S. Malek, T. H. Nguyen, F. Zi, D. S. Scheirer, and H. Müller, Science Advances 5, eaax0800 (2019).
- [18] Y. Bidel, N. Zahzam, A. Bresson, C. Blanchard, M. Cadoret, A. V. Olesen, and R. Forsberg, http://arxiv.org/abs/1910.06666v1.
- [19] B. Barrett, R. Geiger, I. Dutta, M. Meunier, B. Canuel, A. Gauguet, P. Bouyer, and A. Landragin, Comptes Rendus Physique 15, 875 (2014).
- [20] T. L. Gustavson, P. Bouyer, and M. A. Kasevich, Physical Review Letters 78, 2046 (1997).
- 21] J. K. Stockton, K. Takase, and M. A. Kasevich, Physical Review Letters 107 (2011), 10.1103/physrevlett.107.133001

- [22] S. M. Dickerson, J. M. Hogan, A. Sugarbaker, D. M. S. Johnson, and M. A. Kasevich, Physical Review Letters 111 (2013), 10.1103/physrevlett.111.083 minley, Applied Physics Letters 109, 071113 (2016).
- [23] D. Savoie, Fang, M.Altorio, В. L. A. Sidorenkov, R. Geiger, A. Landragin, and Science Advances 4, eaau7948 (2018).
- [24] Y.-J. Chen, A. Hansen, G. W. Hoth, E. Ivanov, B. Pelle, J. Kitching, and E. A. Donley, Physical Review Applied 12 (2019), 10.1103/physrevapplied 120 140 Avinadav, D. Yankelev, O. Firstenberg, and N. David-
- [25] A. Gauguet, В. Canuel, Τ. Lévèque, W. Chaibi, and A. Landragin, Physical Review A **80** (2009), 10.1103/physreva.80.063604.
- [26] A. Sugarbaker, S. M. Dickerson, J. M. Hogan, and M. A. Kasevich, D. M. S. Johnson, Physical Review Letters 111 (2013), 10.1103/physrevlett.111.113002Peters, Applied Physics B 120, 311 (2015).
- [27] B. Canuel, F. Leduc, D. Holleville, A. Gauguet, J. Fils, A. Virdis, A. Clairon, N. Dimarcq, C. J. Bordé, A. Landragin, and P. Bouyer,
- [28] A. V. Rakholia, Η. J. McGuin-G. W. Biedermann, ness, and

- Physical Review Applied 2 (2014), 10.1103/physrevapplied.2.054012.
- [29] G. W. Hoth, B. Pelle, S. Riedl, J. Kitching, and E. A.
- [30] M. Kasevich and Chu, Physical Review Letters 67, 181 (1991).
- [31] D. Yankelev, С. Avinaday, N. David-O. Firstenberg, son. and Physical Review A 100 (2019), 10.1103/physreva.100.023617.
 - son, arXiv http://arxiv.org/abs/1912.12304v1.
- [33] G. W. Hoth, B. Pelle, J. Kitching, and E. A. Donley, in Slow Light, Fast Light, and Opto-Atomic Precision Metrology X, edited by S. M. Shahriar and J. Scheuer (SPIE, 2017).
- [34] V. Schkolnik, B. Leykauf, M. Hauth, C. Freier, and
- [35] R. Karcher, A. Imanaliev, S. Merlet, and F. P. D. Santos, New Journal of Physics 20, 113041 (2018).
- [36] P. Cheiney, L. Fouché, S. Templier, F. Napoli-Physical Review Letters 97 (2006), 10.1103/physrevlett.97.010402 ano, B. Battelier, P. Bouyer, and B. Barrett,
 - Physical Review Applied 10 (2018), 10.1103/physrevapplied.10.03403